





Structure of Quark Star: A Comparative Analysis of Bayesian Inference and Neural Network Based Modeling

Silvia Traversi^{1,2}  and Prasanta Char^{2,3} 

¹ Dipartimento di Fisica e Scienze della Terra, Università di Ferrara, Via Saragat 1, I-44122 Ferrara, Italy

² INFN Sezione di Ferrara, Via Saragat 1, I-44122 Ferrara, Italy; char@fe.infn.it

³ Space sciences, Technologies and Astrophysics Research (STAR) Institute, Université de Liège, Bât. B5a, B-4000 Liège, Belgium

Received 2020 August 5; revised 2020 September 21; accepted 2020 October 1; published 2020 December 7

Abstract

In this work, we compare two powerful parameter estimation methods, namely Bayesian inference and neural network based learning, to study the quark matter equation of state with constant speed of sound parameterization and the structure of the quark stars within the two-family scenario. We use the mass and radius estimations from several X-ray sources and also the mass and tidal deformability measurements from gravitational wave events to constrain the parameters of our model. The results found from the two methods are consistent. The predicted speed of sound is compatible with the conformal limit.

Unified Astronomy Thesaurus concepts: [Nuclear astrophysics \(1129\)](#); [Neutron stars \(1108\)](#); [Bayesian statistics \(1900\)](#); [Neural networks \(1933\)](#)

1. Introduction

The equation of state (EOS) of dense nuclear matter has been the subject of extensive studies throughout the last few decades (Oertel et al. 2017; Baiotti 2019). Still, a consensus has yet to be reached on the composition of matter at densities higher than the nuclear saturation density. In nature, such densities appear only inside the compact remnants formed after the collapse of the core of massive stars ($\gtrsim 8M_{\odot}$). Therefore, observing such objects can be very useful in understanding their interior. Indeed, the increasing number of electromagnetic (EM), such as radio, X-ray, and gravitational wave (GW), observations have provided valuable information on the EOS of such objects (Özel & Freire 2016; Abbott et al. 2017, 2020; Riley et al. 2019). The discoveries of a few pulsars over $2M_{\odot}$ have put stringent constraints on the EOS of supranuclear matter (Demorest et al. 2010; Antoniadis et al. 2013; Fonseca et al. 2016; Arzoumanian 2018; Cromartie et al. 2019). It requires the matter inside such compact stars (CSs) to be stiff to reach such massive stable configurations. On the other hand, the measurement of tidal deformability from the event GW170817 indicates smaller radii for the low mass CSs (Abbott et al. 2019), meaning the EOS is soft at densities corresponding to the low mass configurations.

From the perspective of nuclear physics, the theory of nuclear interaction at such densities is not fully known. Although, it is expected that new strange degrees of freedom should appear in the system as the core densities increase, which in turn would soften the EOS reducing the maximum mass below the observed pulsar masses (Glendenning 2000). The standard way to approach this problem is to introduce repulsive interaction to make the EOS stiffer (Chatterjee & Vidaña 2016). But, this exercise would also make the low-mass stars larger contradicting the GW data. Additionally, quark stars (Qs) made entirely of strange quark matter (SQM) can also exist if it holds true that the Bodmer–Witten hypothesis of the SQM is the most stable state of matter (Bodmer 1971; Witten 1984). But all the CSs cannot be Qs because it is not possible to explain the pulsar glitches

without assuming a star with a crust (Alpar 1987). These observational contradictions affecting our theoretical understanding of dense matter physics have led to the proposition of an alternative scenario, namely the two-family scenario, by which disjointed families of Qs and hadronic stars (HSs) can coexist (Drago et al. 2014a, 2014b, 2016). In this model, the smaller stars are HSs composed of several strange baryons and Δ resonances and the massive stars are the Qs with deconfined quark matter. Other models also exist in the literature concerning two disconnected branches of compact objects, the most popular being the so-called twin-stars solution where the most massive stars are hybrid stars with a sharp phase transition. This branch has the characteristic feature of smaller radii, as opposed to the two-family scenario. In recent years, many analyses have been performed to test the twin-stars model against the observational data (Montaña et al. 2019; Blaschke et al. 2020; Christian & Schaffner-Bielich 2020) and a comparison with the two-family scenario has also been provided in Burgio et al. (2018).

The connection between nuclear physics and astrophysical observations is usually reflected in the one-to-one correspondence between the EOS and the mass–radius ($M-R$) relations, calculated from the Tolman–Oppenheimer–Volkoff (TOV) equations (Oppenheimer & Volkoff 1939; Lindblom 1998). In recent times, tidal deformability (Λ) has also been used as complimentary information to the radius measurements (Hinderer 2008; Damour & Nagar 2009; Hinderer et al. 2010). Therefore, one can also map the EOS to the $M-\Lambda$ relations. The usual strategy to estimate the EOS is to build a model that includes a number of parameters. One can have some knowledge of these parameters a priori from physical considerations. Then, one can systematically update that knowledge with observational data using Bayesian inference methods to analyze posterior distributions of those parameters (Steiner et al. 2010). This is a robust statistical method where one can quantify the feasibility among competing EOS models, the prior dependence on the inference. In reality, the scope of this method is limited due to the existence of only a few observations and

also because the observational points are not distributed optimally throughout the $M - R$ plane in order to probe the whole plausible range of the EOS inside a CS. It is therefore necessary to develop a methodology that is a complimentary approach to the standard parameter estimation method. A machine-learning-based prediction method can be used as an alternative procedure; its application to high energy physics, astrophysical data analysis, and other branches of physics has recently gained momentum. Deep-learning techniques have also used neural networks (NN) specifically to estimate the dense matter EOS (Fujimoto et al. 2018, 2020; Morawski & Bejger 2020). In these studies, a particular parameterization of the EOS, namely piecewise polytropes, has been used to train, validate, and test the NN. In another work, two different learning methods, specifically support vector machine regression and deep-learning utilizing NN, have been compared to study the saturation properties of nuclear matter in terms of nuclear empirical parameters (Ferreira & Providência 2019).

The purpose of the present work is twofold. First, we wish to present a comparative analysis of the Bayesian parameter estimation and NN based prediction. While doing that we also investigate the structure and properties of QSs within the two-family scenario as a follow-up study to our previous work on HSs. The paper is organized as follows. In Section 2, we describe the EOS model for QSs and the calculation of its structure. The sources used and their selection criteria are specified in Section 3. In Sections 4 and 5, we explain our methodology. Finally, in Sections 6 and 7, we discuss our results and summarize.

2. Two-family Scenario and Quark Star

At its core, the two-family scenario utilizes the idea of the absolute stability of the strange quark matter. One can present several arguments based on astrophysical observations to make a case for this idea as explained in Drago et al. (2014a, 2014b). In this scenario, it is possible to get very compact stars, such as hadronic stars, with radii smaller than 12 km as well as very massive stars, such as quark stars, with maximum masses of about $\sim 2.2M_{\odot}$. In a previous work, we explored the parameter space of the relativistic mean field model to build compact hadronic stars (Traversi et al. 2020). In this work, we mainly focus on the quark stars (QS). For simplicity, we take a constant-speed-of-sound EOS for the QSs (Alford et al. 2013; Chamel et al. 2013; Zdunik & Haensel 2013; Drago et al. 2019) in which the relations between the pressure, energy density, and baryon density are as follows,

$$p = c_s^2(e - e_0), \quad (1)$$

$$p = \frac{c_s^2 e_0}{c_s^2 + 1} \left(\left(\frac{n}{n_0} \right)^{c_s^2 + 1} - 1 \right). \quad (2)$$

Here, e_0 and n_0 represent the energy density and the baryon density at zero pressure, respectively. There are three main quantities in this parameterization: the speed of sound (c_s), the n_0 and the energy per baryon $(E/A)_0 = e_0/n_0$. The bounds on the energy per baryon come from the stability of iron nuclei in light of the two-flavor and three-flavor quark matter. The condition for the absolute stability of the three-flavor strange quark matter is $(E/A)_0 < 930$ MeV, whereas to keep the Fe^{56} stable against decaying in two-flavor quark matter

$(E/A)_0 > 830$ MeV (Weissenborn et al. 2011; Drago et al. 2019). Usually, the speed of sound in the hadronic matter is less than $\sqrt{1/3}$ as the EOS is soft, while at high densities in quark matter, theoretical calculations suggest that it should reach the conformal limit of $\sqrt{1/3}$, due to the QCD asymptotic freedom (Bedaque & Steiner 2015). The validity of this limit is presently an object of discussion and it has been tested against the recent observational data of very massive pulsars and the limits on the tidal deformability provided by the GW events (Annala et al. 2020; Reed & Horowitz 2020; Marczenko 2020). We will further investigate this subject in the context of the two-family scenario in a follow-up paper currently in preparation.

2.1. Calculation of the Structure

The configuration of a static and spherically symmetric CS is modeled using the TOV equations of hydrostatic equilibrium as,

$$\frac{dp}{dr} = -(e + p) \frac{m + 4\pi r^3 p}{r(r - 2m)} \quad (3)$$

$$\frac{dm}{dr} = 4\pi r^2 e. \quad (4)$$

Here, $m = m(r)$ is the enclosed gravitational mass at radius r from the center. We integrate Equations 3 and 4 from the center $r = 0$ to the surface of the star at radius R , where $p(R) = 0$, leading to its mass $M = m(R)$. Additionally, we also calculate the tidal deformability of the star, defined as

$$\Lambda = \frac{2}{3} k_2 \left(\frac{R}{M} \right)^5, \quad (5)$$

where k_2 is the electric-type tidal Love number associated with the quadrupolar tidal perturbation, given by the following expression

$$\begin{aligned} k_2 = & \frac{8C^5}{5} (1 - 2C)^2 [2 + 2C(y - 1) - y] \\ & \times \{2C[6 - 3y + 3C(5y - 8)] + 4C^3 \\ & \times [13 - 11y + C(3y - 2) + 2C^2(1 + y)] \\ & + 3(1 - 2C)^2 [2 - y + 2C(y - 1)] \ln(1 - 2C)\}^{-1}. \end{aligned} \quad (6)$$

Here, y is the solution of the following equation at $r = R$,

$$\begin{aligned} \frac{dy}{dr} = & -\frac{y^2}{r} - \frac{r + 4\pi r^3(p - e)}{r(r - 2m)} y + \frac{4(m + 4\pi r^3 p)^2}{r(r - 2m)^2} \\ & + \frac{6}{r - 2m} - \frac{4\pi r^2}{r - 2m} \left[5e + 9p + \frac{e + p}{(dp/de)} \right]. \end{aligned} \quad (7)$$

Since the QSs have a sharp discontinuity of energy density at the surface, the value of $y(R)$ requires a correction term (Hinderer et al. 2010; Postnikov et al. 2010; Takátsy & Kovács 2020) as,

$$y = y(R) - \frac{4\pi R^3 e_-}{M}. \quad (8)$$

Here, e_- is the energy density just inside the surface.

3. Observational Data: Candidate Quark Stars

In this section, we specify the sources used in this work. We select some of the sources from the X-ray measurements of Özel et al. (2016) depending on their masses.⁴ In the context of the two-family scenario, three types of binaries are possible: HS–HS, HS–QS, and QS–QS. An estimate of the threshold mass for a prompt collapse to black hole, M_{thr} , has been provided in De Pietri et al. (2019) for each of the different combinations: in the case of HS–HS we found $M_{\text{thr}} = 2.5M_{\odot}$. Since GW170817 was not a prompt collapse event, we interpret it as an HS–QS merger and thus we classify the high-mass component as a QS and label it as GW170817_1. Then, we marginalize the distribution of the mass of the object from the posterior samples and find the mean value as $1.49M_{\odot}$. Therefore, the sources with the mean of the mass distribution, $M \gtrsim M_{\text{GW170817}_1}$, can be hypothetically identified as QSs. Explicitly, we have considered 4U 1724-07, SAX J1748.9 2021, 4U 1820–30, 4U 1702–429, J0437–4715, GW170817_1, GW190425_1, and GW190425_2. For 4U 1702–429 (Nättälä et al. 2017) and J0437–4715 (Gonzalez-Caniulef et al. 2019), we take the following form of a bivariate Gaussian distribution to mimic the $M - R$ posterior since the full distribution is not available,

$$P(M, R) = \frac{1}{2\pi\sigma_M\sigma_R\sqrt{1-\rho^2}} \times \exp\left\{-\frac{1}{2(1-\rho^2)}\left[\frac{(M-\mu_M)^2}{\sigma_M^2} - 2\rho\frac{(M-\mu_M)(R-\mu_R)}{\sigma_M\sigma_R} + \frac{(R-\mu_R)^2}{\sigma_R^2}\right]\right\}. \quad (9)$$

For 4U 1702–429, we use $\mu_M = 1.9M_{\odot}$, $\mu_R = 12.4$ km, $\sigma_M = 0.3M_{\odot}$, $\sigma_R = 0.4$ km, and $\rho = 0.9$ as before to represent the correlation between the measurements, since these were simultaneous measurements. For J0437–4715, we use $\mu_M = 1.44M_{\odot}$, $\mu_R = 13.6$ km, $\sigma_M = 0.07M_{\odot}$, $\sigma_R = 0.85$ km, and $\rho = 0.0$, since the mass and radius measurements were independent in this case. We have chosen this particular source despite its mass being lower than M_{GW170817_1} , because it has a radius larger than ~ 13 km and HSs in our scheme cannot produce such a large radius. Therefore, it is assumed to be a quark star. For the GW sources, we take the distribution for their individual Λ s directly, because converting to the $M - R$ posterior requires the assumption of certain universal relations, which do not include quarks, and we postulate that all CSs have identical EOSs.⁵

4. Bayesian Inference

We use the Bayesian framework developed in Steiner et al. (2010), Özel et al. (2016), and Raithel et al. (2017). Bayes' theorem tells us that the posterior distribution function (PDF) of a set of parameters (θ_j) given data (D) for a model (M) can be

expressed as,

$$P(\theta_j|D, M) = \frac{P(D|\theta_j, M)P(\theta_j|M)}{P(D|M)}, \quad (10)$$

where $P(\theta_j|M)$ is the prior probability of the parameter set ($\theta_j = e_0, c_s^2$), $P(D|\theta_j, M)$ is the likelihood function of the data given the model, and $P(D|M)$ is known as evidence for the model. For a given data set $P(D|M)$ is a constant and can be treated as a normalization factor. Hence, we have in this case,

$$P(e_0, c_s^2|\text{data}) = CP(\text{data}|e_0, c_s^2)P(e_0)P(c_s^2), \quad (11)$$

where, $P(e_0)$ and $P(c_s^2)$ are the priors over e_0 and c_s^2 ; and

$$P(\text{data}|e_0, c_s^2) = \prod_{i=1}^N P_i(M_i, R_i|e_0, c_s^2) \quad \text{or,} \\ P(\text{data}|e_0, c_s^2) = \prod_{i=1}^N P_i(M_i, \Lambda_i|e_0, c_s^2) \quad (12)$$

is the likelihood of generating N observations given a particular set of EOS parameters. We follow the procedure suggested by Raithel et al. (2017) to calculate the probability of the realization of (M, R) or M, Λ for a particular source given an EOS. We take a set of parameters to construct the EOS, solve the TOV equations and build a $M - R - \Lambda$ sequence up to the maximum mass, which corresponds to the last stable point of the curve. After that, we compute the probability of each configuration of the curve using the $M - R$ or $M - \Lambda$ distribution of the source. Finally, we assign to the parameter set the maximum probability obtained for the configurations as,

$$P_i(M_i, R_i) = P_{\text{max}}(M_i, R_i|e_0, c_s^2, e_c) \quad \text{or,} \\ P_i(M_i, \Lambda_i) = P_{\text{max}}(M_i, \Lambda_i|e_0, c_s^2, e_c), \quad (13)$$

where, the $M - R - \Lambda$ sequence for a given EOS is parameterized by the central energy density (e_c) of the star. We use the Markov Chain Monte Carlo (MCMC) simulations to populate the posterior distribution of Equation (11) using the python based software `emcee` with the stretch-move algorithm (Foreman-Mackey et al. 2013).

5. Deep Learning

The deep-learning method is used to create complex nonlinear mapping between the input and output. It relies on the NN optimized by a set of training data to be able to predict the most likely output given an input. The advantage of NN to predict the EOS is that the multilayered structure of the NN is capable of reproducing the nonlinear nature of the inversion mapping between the $M - R$ relation and EOS, excluding the uncertainties about the assumption of a fitting function. In this work, we mainly follow the methodology developed in Fujimoto et al. (2018, 2020) in constructing the NN and preparing the data. The model function of the NN can be written as:

$$y_i^{(k+1)} = f^{(k+1)}\left(\sum_{j=1}^{N_k} W_{ij}^{(k+1)}y_j^{(k)} + a_i^{(k+1)}\right). \quad (14)$$

Here we have, the k -th layer containing N_k numbers of neurons, $y_j^{(k)}$ are the values stored at the neurons at the k -th layer,

⁴ The $M-R$ distributions of the sources of Özel et al. (2016) are available at <http://xtreme.as.arizona.edu/neutronstars/>.

⁵ The data from GW170817 and GW190425 are available at <https://dcc.ligo.org/LIGO-P1800115/public> and, <https://dcc.ligo.org/LIGO-P2000026/public>.

Table 1
Construction of the NN in This Study

Layer Index	Nodes	Activation
0	16	N/A
1	50	ReLU
2	50	ReLU
3	50	ReLU
4	1/2	tanh

Note. 16 neurons at the input layer correspond to five pairs of mass and radius and three pairs of mass and tidal deformability.

$\{W_{ij}^{(k)}, a_i^{(k)}\}$ being the weights and biases, respectively, on the k -th layer, and finally, the $f^{(k)}$ being the so-called activation functions. These transformations are applied iteratively between subsequent layers. For the optimization procedure, a loss function can be chosen and thus minimized.

5.1. Preparation of Training, Validation, and Test Data

We follow a procedure similar to that described in Fujimoto et al. (2018, 2020) to generate the training and validation data set. We randomly select a number (N_{EOS}) of parameter sets for which we construct the EOSs and calculate the $M - R - \Lambda$ sequences. Since our quark stars should be massive, we keep in the sequence only the stars with masses within $[1.3M_{\odot}, M_{\text{max}}]$. Next, we sample a total of eight data points, representing the sources described in Equation 3, from a uniform distribution of M over the remainder of the sequence. We now have five points of (M_i^0, R_i^0) and three points of (M_i^0, Λ_i^0) . Now, for the network to learn the observational errors associated with the sources and connect with the true sequence, one has to introduce certain shifts on the bare value of the parameters. Since we already have a set of (σ_M, σ_R) and $(\sigma_M, \sigma_{\Lambda})$ after marginalization of the observational data, we build Gaussian distributions for the mass with mean at M_i^0 and standard deviation σ_M^i , for the radius with mean at R_i^0 and standard deviation σ_R^i , and for the tidal deformability with mean at Λ_i^0 and standard deviation σ_{Λ}^i . From these distributions, we sample five new pairs of (M_i, R_i) and three pairs of (M_i, Λ_i) . In this way, we take into account the observational errors of the real data. Now, for each of the selected EOSs, we repeat the last step a large number of times (N_s) and finally produce $N_{\text{EOS}} \times N_s$ numbers of training data. Each of these data points is a vector of 16 entries that comprises masses, radii, and tidal deformabilities $(M_i, M_j, R_i, \Lambda_j; i = 1, 2, \dots, 5; j = 6, 7, 8)$. For the validation and the test set, we repeat the same exercise but with smaller N_{EOS} and $N_s = 1$. The final size of our training data set is 2000×100 in the case of 1D and $10,000 \times 100$ for 2D while the validation and test set in both cases are 1000×1 . Once the network is trained, it should be able to give the value of the parameters of the real EOS starting from the mean values of the marginalized distributions of the masses and radii/tidal deformabilities of the selected sources.

5.2. Features of the Neural Network

Here, we specify the details of the NN used in this calculation. We use the Python package Keras (Chollet 2015) using TensorFlow (Abadi et al. 2016) as a backend and

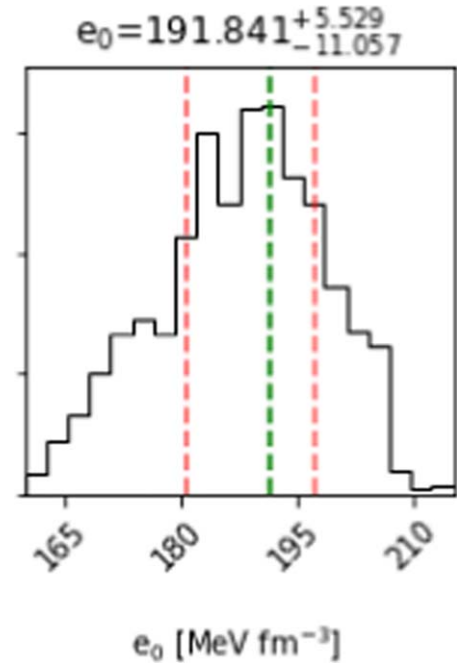


Figure 1. PDF for the parameter e_0 from the Bayesian analysis. The green line is placed on the mode of the distribution, while the red line represents the 68% CI.

Table 2
Features of the Most Probable EOS Obtained with the Bayesian analysis (Bayes) and the NN Method (NN) in the One Parameter (1P) and Two Parameter (2P) Cases

	Bayes 1P	NN 1P	Bayes 2P	NN 2P
e_0 (MeV fm $^{-3}$)	191.84	191.04	183.48	191.29
c_s^2	1/3	1/3	0.306	0.38
$M_{\text{max}} (M_{\odot})$	2.18	2.19	2.13	2.37
$R_{M_{\text{max}}} \text{ (km)}$	12.01	12.03	12.00	12.42
$R_{1.6} \text{ (km)}$	12.10	12.12	12.20	12.26
$\Lambda_{1.6}$	368	373	382	417

Note. The inferred values are specified together with the corresponding maximum mass (M_{max}) star and its radius ($R_{M_{\text{max}}}$) and for the $1.6M_{\odot}$ configuration, the radius ($R_{1.6}$), and the tidal deformability ($\Lambda_{1.6}$).

Scikit-learn (Pedregosa et al. 2011). The structure of our network is summarized in Table 1.

So, the input layer contains the same number of neurons as the observed parameters of the sources (16, in this case). The output layer contains the number of neurons as the number of the EOS parameters (one or two depending on our choice of QS EOS). For the training, validation, and test data, we use the “StandardsScaler” function of Scikit-learn to normalize the observational part and the EOS part is normalized with uniform normalization ($y_{\text{norm}} = \frac{y - y_{\text{min}}}{y_{\text{max}} - y_{\text{min}}}$).

We select the activation function “tanh” for the output layer to get a normalized output that can be converted to our desired parameter values afterwards. For the internal layers, we use the

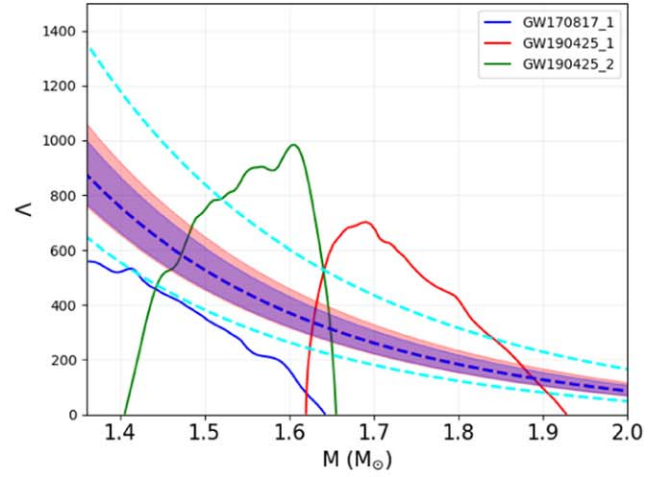
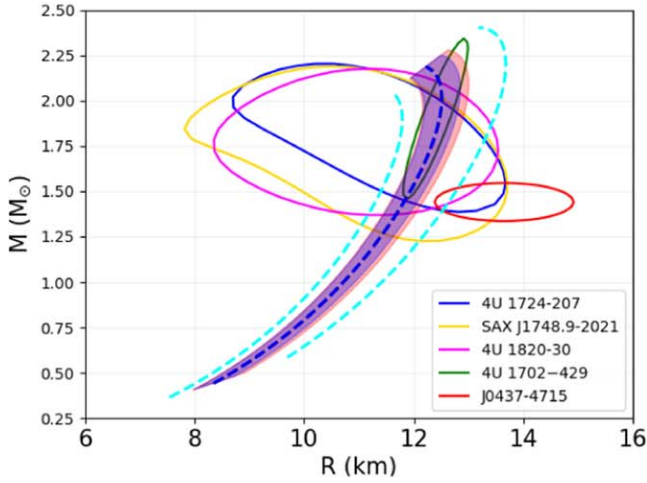


Figure 2. Comparison between the M - R (left) and M - λ curves obtained with the two methods employed. The red and blue shaded regions correspond to the 68% CI predicted by the Bayesian analysis and NN, respectively. The two most probable configurations, which are indistinguishable, are plotted as the dashed blue line. Finally, the dashed cyan lines represent the border of the allowed parameter space.

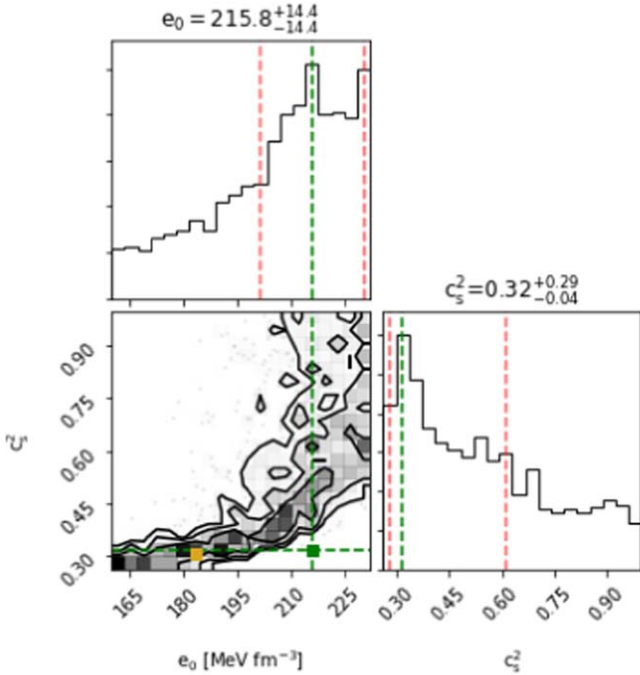


Figure 3. Joint PDF from the Bayesian analysis for the parameters e_0 and c_s^2 , as well as the marginalized distributions, where the green lines are placed on the modes and the red line represents the 68% CI. The yellow point indicates the maximum of the 2D posterior.

standard “ReLU” function. We choose mean-squared logarithmic error (MSLE) as the loss function.

$$MSLE = \frac{1}{m} \sum_{i=1}^m (\ln(y^i + 1) - \ln(y_p^i + 1))^2, \quad (15)$$

where y are the labels, i.e., the real values of the parameters, and y_p are the predicted values. We use the standard “Adam” optimization method (Kingma & Ba 2014) along with mini-batch size 128. Finally, the NN parameters are initialized with Glorot uniform distribution (Glorot & Bengio 2010). For the two-parameter EOS calculation, the “l2” regularization is used. The learning rate is taken as $\alpha = 0.005$. Due to the limitation of the computational resources, we have not performed the

hyperparameter tuning, which we have set aside as a future exercise.

The uncertainties in the NN prediction can be estimated using the rms error $\left(RMSE = \sqrt{\frac{\sum_{i=1}^m (y^i - y_p^i)^2}{m}} \right)$ estimated on the test set. For the 2D case, we find RMSEs separately for each of the parameters then we built a 2D Gaussian using the RMSEs as sigmas. Then, we take the 68% CI from that distribution and calculate the corresponding quantities.

6. Results and Discussion

We present our results for Bayesian and NN calculations following the methodology developed in Equations 4 and 5, respectively, for two cases in separate subsections, first keeping the c_s^2 fixed, only varying the e_0 , and then varying both of them. The goal is to understand which value of the squared speed of sound is the most suitable to describe the observational data within our model. Then, we check whether or not our result is able to fulfill the conformal limit suggested by QCD calculations.

As the most massive pulsar discovered until now has a mass of $2.14_{-0.09}^{+0.10}$ (Cromartie et al. 2019), we put a strict lower limit of $2.05M_\odot$ for the maximum mass in our calculation. We use all the sources listed in Section 3. Table 2 summarizes our results concerning the most probable EOSs. We use the python `corner.py` package to visualize one- and two-dimensional projection plots of the samples (Foreman-Mackey 2016).

6.1. One Parameter Case: e_0

This is the simplest case in our analysis with only one parameter. The prior range for e_0 is between 160 and 232 MeV fm^{-3} , which corresponds to the allowed interval in $(E/A)_0$ for the Witten hypothesis to hold true. In this case, we have fixed $c_s^2 = 1/3$. Values of e_0 larger than about 220 MeV fm^{-3} , corresponding to the softest EOSs, are automatically ruled out by the maximum mass limit. In Figure 1, we have shown the most probable value of e_0 along with the 1σ error from the Bayesian calculation. The distribution peaks at 191.841 MeV fm^{-3} . The maximum mass for the sequence corresponding to most probable value of e_0 is $2.18M_\odot$ and the radius of the $1.6M_\odot$ configuration is $R_{1.6} = 12.10$ km.

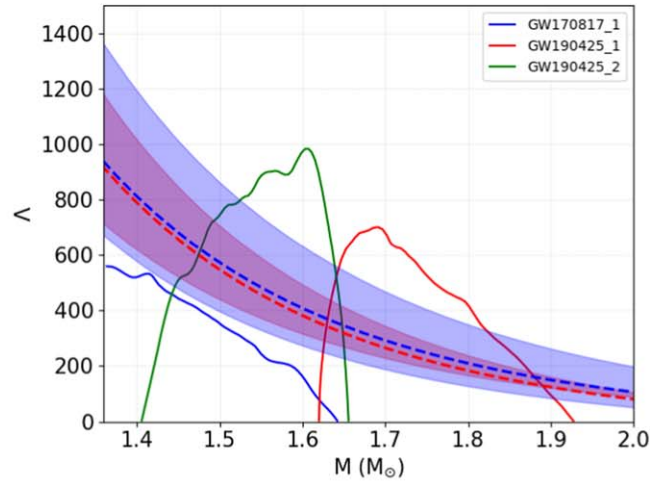
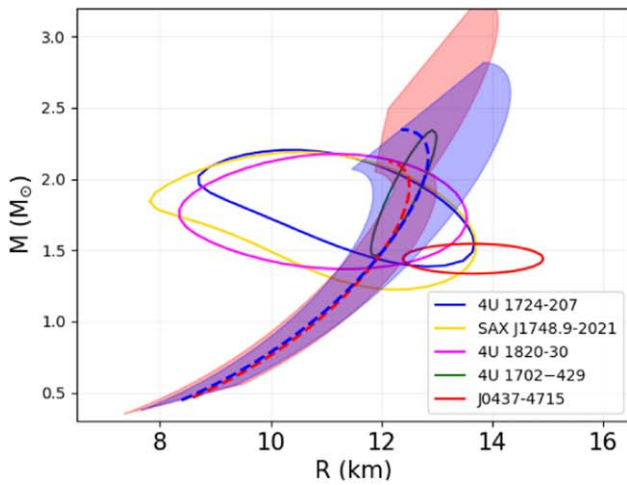


Figure 4. Comparison between the M - R (left) and M - Λ curves obtained with the two methods employed. The red and blue shaded regions correspond to the 68% CI predicted by the Bayesian analysis and NN, respectively. The two most probable configurations are plotted as the dashed red (Bayes) and blue (NN) lines.

From the trained NN, we get the predicted value for e_0 as $191.04 \text{ MeV fm}^{-3}$, almost equivalent to the previous one, with the error $\text{RMSE} = 10.03 \text{ MeV fm}^{-3}$ estimated on the test set. The corresponding M_{max} is $2.19M_{\odot}$ and the $R_{1.6} = 12.12 \text{ km}$. In Figure 2, we compare the $M - R$ and $M - \Lambda$ plots with the values from the 68% confidence interval (CI) of the posterior distribution from the Bayesian calculation (shaded red) and NN predicted (shaded blue) range. The dashed cyan line corresponds to the initial range of the parameter used in both calculations. The most probable configuration from the Bayesian inference coincides with the predicted value from the NN (dashed blue) and the errors are also quite similar. Also in both cases the maximum masses achieved from the most probable parameters are consistent with presently accepted values (Rezzolla et al. 2018). The result is exactly what we expect while comparing both methods.

At the 68% level, these results are not in agreement with the source J0437-4715 and also the GW170817_1. While GW170817_1 indicates a smaller radius, J0437-4715 directs toward a bigger radius.

6.2. Two Parameter Case: e_0 and c_s^2

Next we present the case in which we characterize the speed of sound as a free parameter and try to find out how far its value can deviate from the conformal limit given the present data. We build a joint posterior for e_0 and c_s^2 given the priors on e_0 between 160 and 232 MeV fm^{-3} , same as before, and for c_s^2 , the range $[0.1, 1]$. In this case, the interval in e_0 is not reduced a priori by means of the maximum mass limit, since an increase of the sound speed also allows configurations with $e_0 > 220 \text{ MeV fm}^{-3}$ to reach masses larger than $2.05M_{\odot}$. On the contrary, the maximum mass constraint imposes a lower bound for c_s^2 at about 0.26. In Figure 3, we present the marginalized PDFs for e_0 and c_s^2 along with the most probable values and 1σ errors, while in the 2D projection plot 1σ (39.3%), 68% and 90% CI are shown. The posterior reveals a correlation among the parameters. We find two classes of solutions with low and high values of (e_0, c_s^2) . The second class of values are inside the 68% CI albeit individually less probable from the low (e_0, c_s^2) points. For this reason, the marginalized distributions of e_0 peaks at a value that is quite distant from the high probability region of the 2D PDF. The most probable point of the

joint PDF is at $e_0 = 183.48 \text{ MeV fm}^{-3}$, $c_s^2 = 0.306$, but we also find other points with very similar probabilities close to the maximum. These two different classes are also found in the $M - R$ sequences in Figure 4. The first one is characterized by not too large maximum masses ~ 2.1 – $2.2M_{\odot}$ and radii in the range $R_{1.6} \sim 11.6$ – 12.9 km allowing the 68% CI to overlap also with J0437-4715. On the other hand, the second type of solutions can reach both very big maximum mass up to $\sim 3.25M_{\odot}$ and quite small radii $R_{1.6} \lesssim 11.7 \text{ km}$. The preferred solution, represented with a red dashed line in Figure 4, belongs to the first class and thus the conformal limit on c_s is fulfilled. We obtained for this EOS $M_{\text{max}} = 2.13M_{\odot}$ and $R_{1.6} = 12.20 \text{ km}$.

Concerning the NN results, the optimal values are $e_0 = 191.29 \text{ MeV fm}^{-3}$, $c_s^2 = 0.38$. Although this point does not exactly correspond to the absolute peak in the Bayesian posterior, it is one of the multiple high probability modes of the distribution and it is located well inside the largest likelihood region. The reason for the existence of many relevant combinations of parameters all belonging to the low (e_0, c_s^2) class is that the $M - R$ sequences corresponding to each of them coincide for most of the sequences. This appears evident from the red and blue dashed lines of Figure 4 representing the preferred EOSs found using the two approaches. The NN curve is indeed characterized by an $R_{1.6} = 12.26$ but with a larger maximum mass $M_{\text{max}} = 2.37M_{\odot}$. We underline that for a total mass as that of GW190425 and the preferred parameters found in this analysis, a prompt collapse is expected for a double QSs binary. Similar to the 1P case, our results in the $M - R$ and $M - \Lambda$ planes are not in agreement with the 68% CI of the GW170917_1 PDF and only marginally compatible with the source J0437-4715.

After the training, The RMSEs of the NN found on the test set are 15.5 MeV fm^{-3} for e_0 and 0.13 for c_s^2 . As mentioned before, the error is estimated as the 68% CI of the 2D Gaussian built from the single RMSEs on the parameters. This approximation is the main limitation of our NN approach: the absence of an explicit probability distribution prevents the correlation between e_0 and c_s^2 to be seen. As a consequence, we cannot find the two types of solutions provided by the Bayesian method and the 68% CIs in the M - R and M - Λ planes are considerably larger.

7. Summary and Conclusions

In this work, we parameterized the QS EOS adopting a constant-speed-of-sound model with two parameters (c_s^2 , e_0). We used $M - R$ posteriors of several X-ray sources and Λ posteriors from GW events to estimate the most probable values of those parameters using both Bayesian inference and NN prediction methods. For the NN calculations, we used marginalized Gaussians when incorporating the observational errors. While we have found that results from these two methods are in agreement with each other, from the construction of our NN we do not find any correlation between the predicted parameters. In contrast to the previous works of Fujimoto et al. (2018, 2020), we have tried to provide a quantitative comparison between these two methods given the QS EOS model. We have also included the tidal deformabilities at the same level of radius without converting it into other equivalent quantities while performing the NN predictions as done in Morawski & Bejger (2020). Both methods predict inconsistency of our EOS model with the sources GW170817_1 and J0437–4715 at the 68% level although other sources used in the studies are compatible with the predictions. The compatibility found between the estimated parameter values from those two methods motivates us to recognize the NN based prediction as an efficient complimentary method to the standard Bayesian calculation. One of the criticisms of this work can be the way we have incorporated the uncertainties of the measurements in the NN framework. Ideally, one would prefer to use the full distribution instead of a double Gaussian with marginalized data. One of our future plans is to determine a computationally efficient procedure to include the comprehensive data sets. This will automatically include the correlation between the $M - R$ and $M - \Lambda$ measurements of the sources.

Moreover, we plan to improve our NN method to include a study of the correlations in our parameter space and therefore to obtain a better estimate of the errors.

We would like to thank Giuseppe Pagliara and Alessandro Drago for useful discussions. P.C. acknowledges support from INFN postdoctoral fellowship. P.C. is supported by the Fonds de la Recherche Scientifique-FNRS, Belgium, under grant No. 4.4503.19.

Software: Keras (Chollet 2015), TensorFlow (Abadi et al. 2016), Scikit-learn (Pedregosa et al. 2011), corner.py (Foreman-Mackey 2016), emcee (Foreman-Mackey et al. 2013).

ORCID iDs

Silvia Traversi  <https://orcid.org/0000-0002-8410-520X>
Prasanta Char  <https://orcid.org/0000-0001-6592-6590>

References

Abadi, M., Barham, P., Chen, J., et al. 2016, in 12th USENIX Symp. on Operating Systems Design and Implementation, OSDI 16 (Berkeley, CA: USENIX), 265
Abbott, B. P., Abbott, R., Abbott, T. D., et al. 2017, *PhRvL*, **119**, 161101
Abbott, B. P., Abbott, R., Abbott, T. D., et al. 2019, *PhRvX*, **9**, 011001

Abbott, B. P., Abbott, R., Abbott, T. D., et al. 2020, *ApJL*, **892**, L3
Alford, M. G., Han, S., & Prakash, M. 2013, *PhRvD*, **88**, 083013
Alpar, M. 1987, *PhRvL*, **58**, 2152
Annala, E., Gorda, T., Kurkela, A., Nättilä, J., & Vuorinen, A. 2020, *NatPh*, **16**, 907
Antoniadis, J., Freire, P. C. C., Wex, N., et al. 2013, *Sci*, **340**, 6131
Arzoumanian, Z., Brazier, A., Burke-Spolaor, S., et al. 2018, *ApJS*, **235**, 37
Baiotti, L. 2019, *PrPNP*, **109**, 103714
Bedaque, P., & Steiner, A. W. 2015, *PhRvL*, **114**, 031103
Blaschke, D., Ayriyan, A., Alvarez-Castillo, D. E., & Grigorian, H. 2020, *Univ*, **6**, 81
Bodmer, A. R. 1971, *PhRvD*, **4**, 1601
Burgio, G. F., Drago, A., Pagliara, G., Schulze, H. J., & Wei, J. B. 2018, *ApJ*, **860**, 139
Chamel, N., Fantina, A. F., Pearson, J. M., & Goriely, S. 2013, *A&A*, **553**, A22
Chatterjee, D., & Vidiya, I. 2016, *EPJA*, **52**, 29
Chollet, F. 2015, Keras, <https://github.com/fchollet/keras>
Christian, J.-E., & Schaffner-Bielich, J. 2020, *ApJL*, **894**, L8
Cromartie, H. T., Fonseca, E., Ransom, S. M., et al. 2019, *NatAs*, **4**, 72
Damour, T., & Nagar, A. 2009, *PhRvD*, **80**, 084035
De Pietri, R., Drago, A., Feo, A., et al. 2019, *ApJ*, **881**, 122
Demorest, P., Pennucci, T., Ransom, S., Roberts, M., & Hessels, J. 2010, *Natur*, **467**, 1081
Drago, A., Lavagno, A., & Pagliara, G. 2014a, *PhRvD*, **89**, 043014
Drago, A., Lavagno, A., Pagliara, G., & Pigato, D. 2014b, *PhRvC*, **90**, 065809
Drago, A., Lavagno, A., Pagliara, G., & Pigato, D. 2016, *EPJ*, **A52**, 40
Drago, A., Moretti, M., & Pagliara, G. 2019, *AN*, **340**, 189
Ferreira, M., & Providência, C. 2019, arXiv:1910.05554
Fonseca, E., Pennucci, T. T., Ellis, J. A., et al. 2016, *ApJ*, **832**, 167
Foreman-Mackey, D. 2016, *JOSS*, **2016**, 24
Foreman-Mackey, D., Hogg, D. W., Lang, D., & Goodman, J. 2013, *PASP*, **125**, 306
Fujimoto, Y., Fukushima, K., & Murase, K. 2018, *PhRvD*, **98**, 023019
Fujimoto, Y., Fukushima, K., & Murase, K. 2020, *PhRvD*, **101**, 054016
Glendenning, N. K. 2000, Compact Stars (2nd edn; Berlin: Springer)
Glorot, X., & Bengio, Y. 2010, in Proc. Machine Learning Research, Vol. 9, Proc. Thirteenth Int. Conf. on Artificial Intelligence and Statistics, ed. Y. W. Teh & M. Titterton (Chia Laguna Resort, Sardinia, Italy: PMLR), 249, <http://proceedings.mlr.press/v9/glorot10a.html>
Gonzalez-Caniulef, D., Guillot, S., & Reisenegger, A. 2019, arXiv:1904.12114
Hinderer, T. 2008, *ApJ*, **677**, 1216
Hinderer, T., Lackey, B. D., Lang, R. N., & Read, J. S. 2010, *PhRvD*, **81**, 123016
Kingma, D. P., & Ba, J. 2014, arXiv:1412.6980
Lindblom, L. 1998, *PhRvD*, **58**, 024008
Marczenko, M. 2020, arXiv:2005.14535
Montaña, G., Tolos, L., Hanauske, M., & Rezzolla, L. 2019, *PhRvD*, **99**, 103009
Morawski, F., & Bejger, M. 2020, *A&A*, **642**, 78
Nättilä, J., Miller, M. C., Steiner, A. W., et al. 2017, *A&A*, **608**, A31
Oertel, M., Hempel, M., Klähn, T., & Typel, S. 2017, *RvMP*, **89**, 015007
Oppenheimer, J. R., & Volkoff, G. M. 1939, *PhRv*, **55**, 374
Özel, F., & Freire, P. 2016, *ARA&A*, **54**, 401
Özel, F., Psaltis, D., Guver, T., et al. 2016, *ApJ*, **820**, 28
Pedregosa, F., Varoquaux, G., Gramfort, A., et al. 2011, Journal of Machine Learning Research, **12**, 2825, <https://www.jmlr.org/papers/volume12/pedregosa11a/pedregosa11a.pdf>
Postnikov, S., Prakash, M., & Lattimer, J. M. 2010, *PhRvD*, **82**, 024016
Raithel, C. A., Özel, F., & Psaltis, D. 2017, *ApJ*, **844**, 156
Reed, B., & Horowitz, C. 2020, *PhRvC*, **101**, 045803
Rezzolla, L., Most, E. R., & Weih, L. R. 2018, *ApJL*, **852**, L25
Riley, T. E., Watts, A. L., Bogdanov, S., et al. 2019, *ApJL*, **887**, L21
Steiner, A. W., Lattimer, J. M., & Brown, E. F. 2010, *ApJ*, **722**, 33
Takátsy, J., & Kovács, P. 2020, *PhRvD*, **102**, 028501
Traversi, S., Char, P., & Pagliara, G. 2020, *ApJ*, **897**, 165
Weissenborn, S., Sagert, I., Pagliara, G., Hempel, M., & Schaffner-Bielich, J. 2011, *ApJL*, **740**, L14
Witten, E. 1984, *PhRvD*, **30**, 272
Zdunik, J., & Haensel, P. 2013, *A&A*, **551**, A61